



Unraveling magneto-elastoresistance in the Dirac nodal-line semi-metal ZrSiSe



J. F. Linnartz¹ ✉, A. Kool¹ , J. P. Lorenz² , C. S. A. Müller¹ , M. R. van Delft¹ , R. Singha^{3,4} , L. M. Schoop³ , N. E. Hussey^{1,5} , A. de Visser² & S. Wiedmann¹ ✉

Quantum materials are often characterized by a marked sensitivity to minute changes in their physical environment, a property that can lead to new functionalities and thereby, to novel applications. One such key property is the magneto-elastoresistance (MER), the change in magnetoresistance (MR) of a metal induced by uniaxial strain. Understanding and modeling this response can prove challenging, particularly in systems with complex Fermi surfaces. Here, we present a thorough analysis of the MER in the nearly compensated Dirac nodal-line semi-metal ZrSiSe. Small amounts of strain (0.27%) lead to large changes (7%) in the MR. Subsequent analysis reveals that the MER response is driven primarily by a change in transport mobility that varies linearly with the applied strain. This study showcases how the effect of strain tuning on the electrical properties can be both qualitatively and quantitatively understood. A complementary Shubnikov-de Haas oscillation study sheds light on the root of this change in quantum mobility. Moreover, we unambiguously show that the Fermi surface consists of distinct electron and hole pockets revealed in quantum oscillation measurements originating from magnetic breakdown.

The application of uniaxial strain has proven to be a valuable tool to investigate novel phenomena in various quantum materials over the past 20 years, including iron-based superconductors¹, narrow gap materials, such as ZrTe₅² and charge density wave systems³, all using commercially available strain cell⁴. The technique is maturing, having been combined with techniques as diverse as μ SR⁵, electrocaloric effect⁶, and Raman spectroscopy⁷. Despite these developments, the vast majority of strain-induced studies have focused on the magnetotransport response, and in particular, the magnetoresistance (MR) or magneto-elastoresistance (MER).

Over the last few years, two types of MR are of particular interest. Firstly, a linear-in-field MR, which can be found, for instance, in correlated electron systems^{8,9} or confined systems¹⁰, and, secondly, a large quadratic and non-saturating MR^{11–15} that can reach values of over 10⁸%^{16,17}. Non-saturating quadratic MR can be explained, for example, by an open Fermi surface (FS) or by an equal or nearly equal amount of electron and hole quasi-particles in a material¹⁸. It is this non-saturating large MR and the peculiar FS of compensated semi-metals consisting of small electron and hole pockets, that makes them particularly susceptible to external tuning parameters such as uniaxial strain^{19,20}.

The material under study, ZrSiSe, is a member of the Dirac nodal-line semi-metal family^{21–27}. Its FS has been investigated by magneto-transport

measurements and quantum oscillation (QO) experiments^{28–32}, providing evidence for its topological character. However, the exact topology of the FS of ZrSiSe is questioned and different realizations can be found in literature^{28–39}. An external tuning parameter like strain may help to shed light on the precise geometry and topology of the FS. Theoretical works have also proposed the existence of correlation effects^{33,34} and the material's tunability under the application of strain while its topology remains protected³⁵.

In this work, we present the low-temperature magneto-transport of ZrSiSe under uniaxial strain in magnetic fields up to 30 T where we see a change of the MR up to 7%. MR is defined as, $MR = (R(B) - R(0))/R(0)$, where $R(B)$ and $R(0)$ are the resistances measured at finite and zero B , respectively. We show this change is consistent for a multitude of samples, cut along the [100] and [110] directions. The sample notation denotes both the current/voltage path and the straining direction. By analyzing the MER as a function of the magnetic field (B), we demonstrate that MER can originate either from a deviation of perfect charge carrier compensation or changes in the transport mobility of the quasi-particles using a standard two-carrier Drude model; the latter being applicable to ZrSiSe. Furthermore, from the analysis of Shubnikov-de Haas (SdH) QOs, we identify strain-induced changes in the quantum

¹High Field Magnet Laboratory (HFML-EMFL) & Institute for Molecules and Materials, Radboud University, Nijmegen, The Netherlands. ²Van der Waals-Zeeman Institute, University of Amsterdam, Amsterdam, The Netherlands. ³Department of Chemistry, Princeton University, Princeton, NJ, USA. ⁴Department of Physics, Indian Institute of Technology Guwahati, Guwahati, India. ⁵H.H. Wills Physics Laboratory, University of Bristol, Bristol, UK. ✉e-mail: jasper.linnartz@ru.nl; steffen.wiedmann@ru.nl

mobility and the tunneling gap between electron and hole pockets in momentum space.

Our analysis demonstrates how one is able to identify which parameters are tuned under strain in compensated systems by following the field-dependent changes in MR. Directly from the signature of the MER, changes in compensation and/or mobility can be distinguished as well as direct visualization of how much the mobility is changing. ZrSiSe is chosen as the material to showcase the strengths of this MER analysis. The simplicity of the model is able to capture the underlying physics correctly, such that, strain-induced changes in physical parameters are directly exposed.

Results and discussion

Magneto-transport up to 30 T

Figure 1 shows a zero- and high-field transport characterization of our ZrSiSe crystals. In Fig. 1a, the longitudinal resistance, R_{xx} , is shown as a function of temperature T for sample S2[110]. Figure 1b summarizes $R_{xx}(B)$ for all samples measured up to 30 T at 1.3 K showing an increasing MR superimposed by SdH QOs. The inset highlights two samples with their B^2 -dependence of the MR for S2[110] and S2[100]. In the following section, we focus on the analysis of the MR for S2[110] and the QO pattern for S2[100]. These samples show the largest MR ($7.8 \times 10^3\%$ at 9 T) and most pronounced QOs, respectively. Panels (c) and (d) of Fig. 1 show the temperature-dependent MR for sample S2[100]. In Fig. 1d, in a field range $27 \text{ T} < B < 30 \text{ T}$, high-frequency QOs are observed at low temperatures corresponding to magnetic breakdown (MB) in the ZRA-plane of the FS, as previously found in ZrSiS^{40,41} and HfSiS^{42,43}, but not yet in ZrSiSe.

MR and MER

We now focus on the effect of uniaxial strain ϵ on the MR. A precise description of MER and magneto-elasticity is presented in Supplementary Note 1. The MR in the most simple (compensated) semi-metallic system is due to a single electron-like and a single hole-like FS. The MR of such a semimetal can be expressed by $\text{MR} = [(\rho_{xx}(B) - \rho_{xx}(0))/\rho_{xx}(0)] \propto (\mu_m)^2 B^2$ with $\mu_m = \sqrt{\mu_e \cdot \mu_h}$ where the mobilities $\mu \propto \tau$ are the average mobilities and transport scattering times, respectively.

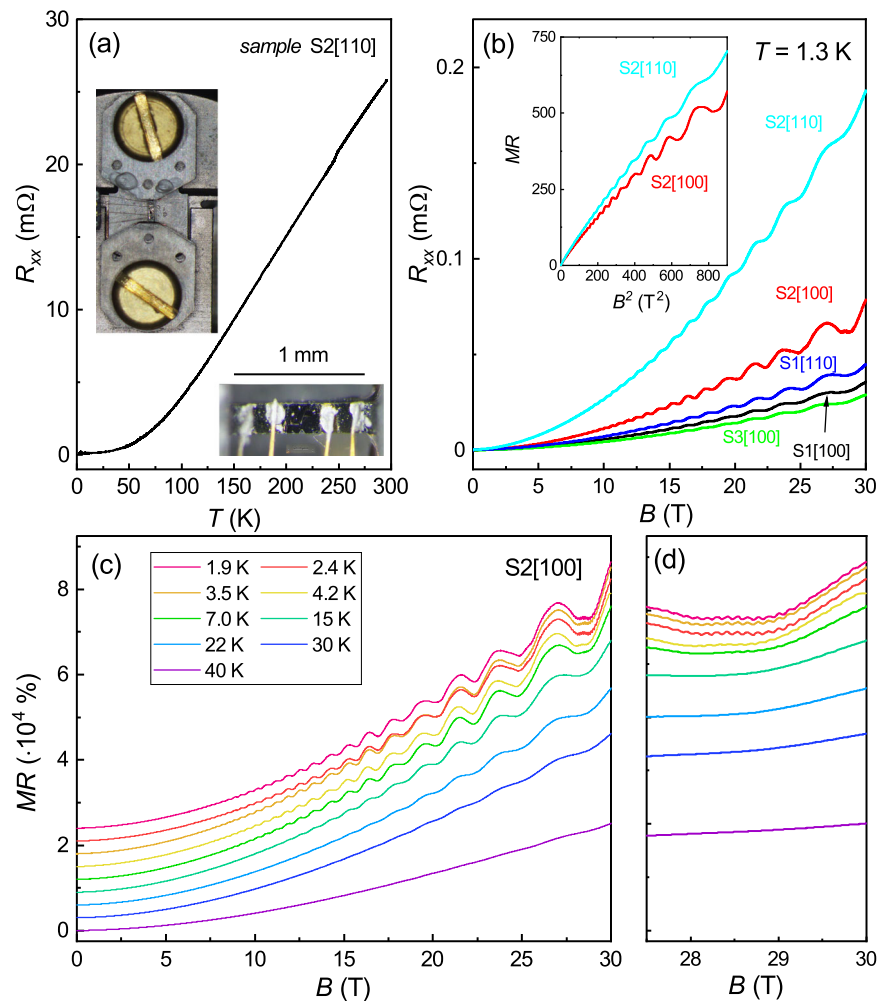
In Fig. 2a the longitudinal resistance of S2[110] R_{xx} is presented for different uniaxial strain values at 1.4 K. It shows a continuous decrease from $\sim 0.3\%$ tensile to $\sim -0.3\%$ compressive strain. The experimental results obtained with strain applied along the [100] and [110] directions show similar behavior in the MR. Clear changes in the QO spectrum are observed and will be discussed in the next section. In Fig. 2b, $\Delta R(B, \epsilon_{xx})/R(B, \epsilon_{xx} = 0)$ is plotted as a function of ϵ_{xx} at $B = 5 \text{ T}$ and $T = 1.4 \text{ K}$ to illustrate the $+5\%$ change in MR for tensile and -5% change for compressive strain. The absolute change of the zero-field resistivity with uniaxial strain is within the noise level of our transport experiment.

To describe the observed results, we employ a standard two-band Drude model for a compensated semi-metal, in which the longitudinal resistivity is written as

$$\rho_{xx} = \frac{(n\mu_e + p\mu_h) + (n\mu_e\mu_h^2 + p\mu_h^2\mu_e)B^2}{e[(n\mu_e + p\mu_h)^2 + (p - n)^2\mu_e^2\mu_h^2B^2]} \quad (1)$$

Fig. 1 | Transport experiments on ZrSiSe.

a Temperature dependence of R_{xx} for S2[110]. The left inset illustrates the strain cell with the crystal mounted. The lower inset shows the sample with the contacts. **b** R_{xx} as a function of B for all samples. The inset highlights the B^2 dependence for the samples with the largest MR and most pronounced QOs. **c, d** Temperature-dependent MR for sample S2[100] in the entire field range (**c**) and high-field part (**d**) where the MB is found. The curves in (**c, d**) are offset for clarity.



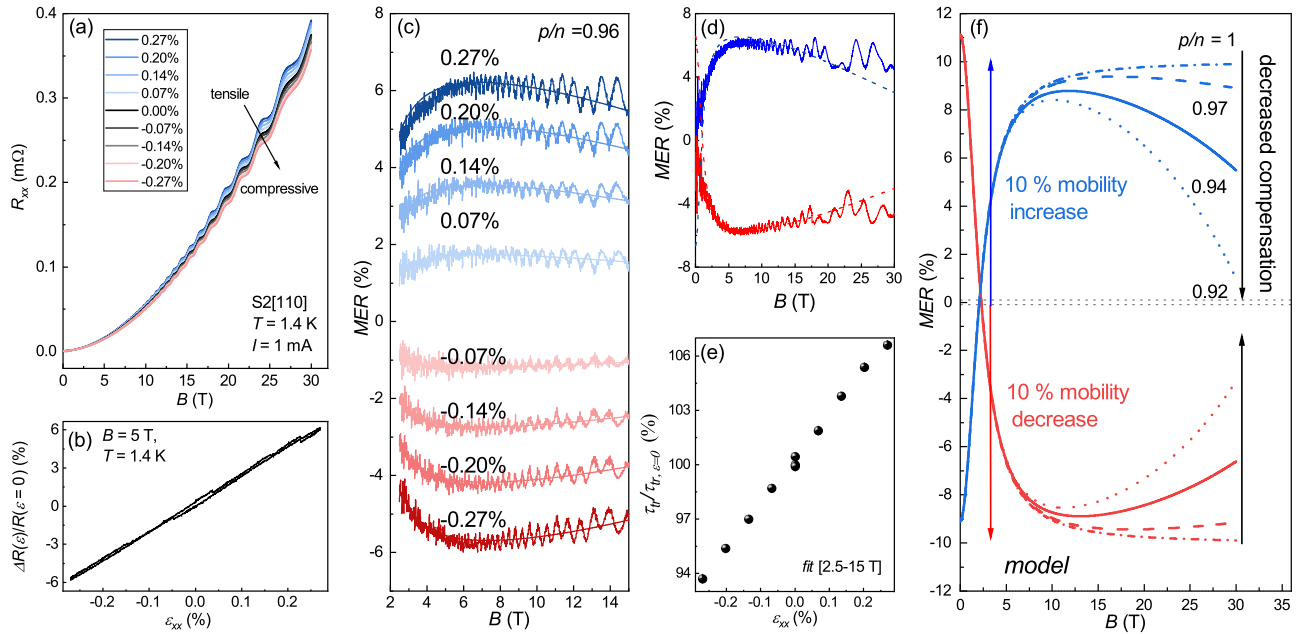


Fig. 2 | MR and MER for S2[110]. **a** R_{xx} as a function of B for different uniaxial strain values applied at 1.4 K. **b** $\Delta R(B, \epsilon_{xx})/R(B, \epsilon_{xx} = 0)$ at 5 T and 1.4 K. **c** MER data and fits for different values of tensile and compressive strain with the fit having a fixed compensation ratio of $p/n = 0.96$. The MER is superimposed by QOs. **d** MER up to

30 T highlighting the deviation at the higher field for the most tensile and compressively strained sweeps. **e** Transport scattering time normalized by the zero strain value as a function of uniaxial strain ϵ_{xx} . **f** MER model for changing carrier mobility ($\pm 10\%$) and different compensation ratios p/n .

and simplifies to

$$\rho_{xx} = \frac{1}{en\mu(1 + p/n)} \frac{1 + \mu^2 B^2}{1 + \frac{(p/n-1)^2}{(p/n+1)^2} \mu^2 B^2} \quad (2)$$

for $\mu = \mu_e = \mu_h$ using the compensation fraction p/n , n (μ_e), and p (μ_h) being the carrier densities (mobilities) for electrons and holes, respectively, and e the absolute electron charge. The MR data for all samples shown in Fig. 1b, were fitted to Eq. (2), and the results are summarized in Supplementary Table 1 and see Supplementary Note 2. From this, we extract a compensation of 0.96 for S2[110]. Typical calculated results for ρ_{xx} as a function of the magnetic field using Eq. (2) are discussed in Supplementary Note 3 and shown in Supplementary Fig. 1.

We now turn our attention to the MER, defined as $MER = (R(B, \epsilon_{xx}) - R(B, 0))/R(B, 0)$. The MER is field-dependent and has a characteristic shape. If the variations in R_{xx} were solely due to changes in sample geometry, the MER would be B -independent and would result in a constant offset of the order of the applied strain. As can be seen in Fig. 2c, however, a clear extremum in the MER is found around 8 T after which the MER converges due to a compensation ratio $p/n \neq 1$. Both the shape and amplitude of the MER provide valuable insights into the underlying physics, as we now show.

Based on the two-band model described in Eq. (2), the effect of strain can be modeled to reconstruct a model MER. Figure 2f shows the field-dependent MER for the case of an arbitrary 10% increase (decrease) in mobility under tensile (compressive) strain for different p/n ratios between 1 and 0.92 as an example. For a perfectly compensated system $p/n = 1$, the MER saturates at higher magnetic fields, and its amplitude (maximum) is given by the absolute change in carrier mobility μ , here 10%. A deviation from perfect compensation leads to a decrease in MER with an increasing magnetic field.

The MER fits to our experiment, as presented in Fig. 2c, are excellent and demonstrate the robustness of this modeling to describe the evolution of the MER. More details about the fits and the fit parameters are given in Supplementary Note 4 and Supplementary Table 2, respectively. A small deviation from the two-band Drude model using $p/n = 0.96$ occurs above

18 T, as shown in Fig. 2d. In Fig. 2e, we plot the transport scattering time, derived from $\mu = e\tau_{tr}/m^*$ with the effective mass m^* , normalized by the zero strain, $\tau_{tr}/\tau_{tr, \epsilon=0}$, as a function of uniaxial strain ϵ_{xx} from the fitting of Fig. 2c. Curiously, the change in the transport lifetime is monotonic in the applied strain, becoming shorter (longer) under compressive (tensile) strain, respectively. In Supplementary Note 5, (Supplementary Figs. 2 and 3), we show additional data on the MR and MER for four samples and various strain values.

It is clear that small amounts of strain can lead to large changes in the MR. While the compensation ratio in ZrSiSe is unaffected by strain, we find that it is the transport mobility that is the root cause of the change in MR. This conclusion could already be reached by understanding the shape of the MER. If the mobility is changing, the extremum of the MER curve is a good indication of the relative change in mobility. The converging behavior after the extremum is by contrast, an indication of the compensation ratio. These changes in transport mobility occur at too low a temperature to be due to a softening of or a reduced coupling to any specific phonon branch. Alternative origins of this anomalous, monotonic change in transport mobility will be discussed having first described the FS deduced from QO studies.

FS quasi-particle properties

Next, we analyze the QO spectrum and strain-induced changes therein. Figure 3 presents the QO spectra (dR_{xx}/dB) for different temperatures as a function of $1/B$ with insets for the high-frequency QOs at the maximum applied strain values. In dR_{xx}/dB we clearly see two distinct characteristics: low-frequency oscillations above 5 T and high-frequency QOs that are well pronounced for $B > 25$ T. The observed frequencies, f , in the FFT spectra, are related to the extremal area A_f of the individual pockets via the Onsager relation $f = (\hbar/2\pi e)A_f$ ⁴⁴. The absence of a change in the observed frequencies immediately excludes changes of the compensation ratio in the MR or MER in the presence of uniaxial strain, see Supplementary Note 6.

We start the discussion by describing the expected FS topology of ZrSiSe. To facilitate our discussion, we focus here on a slice of the FS within the ZRA plane, shown as an inset in Fig. 3b, and consider the low-frequency QOs and their FFTs in the range [7–30 T] for $\epsilon_{xx} = 0$, illustrated in Fig. 3e. We find in total five distinct peaks below 300 T which we label as $f_\delta = 125$ T, $f_\alpha = 210$ T, and $f_1 = 265$ T. In addition, we find two frequencies located at

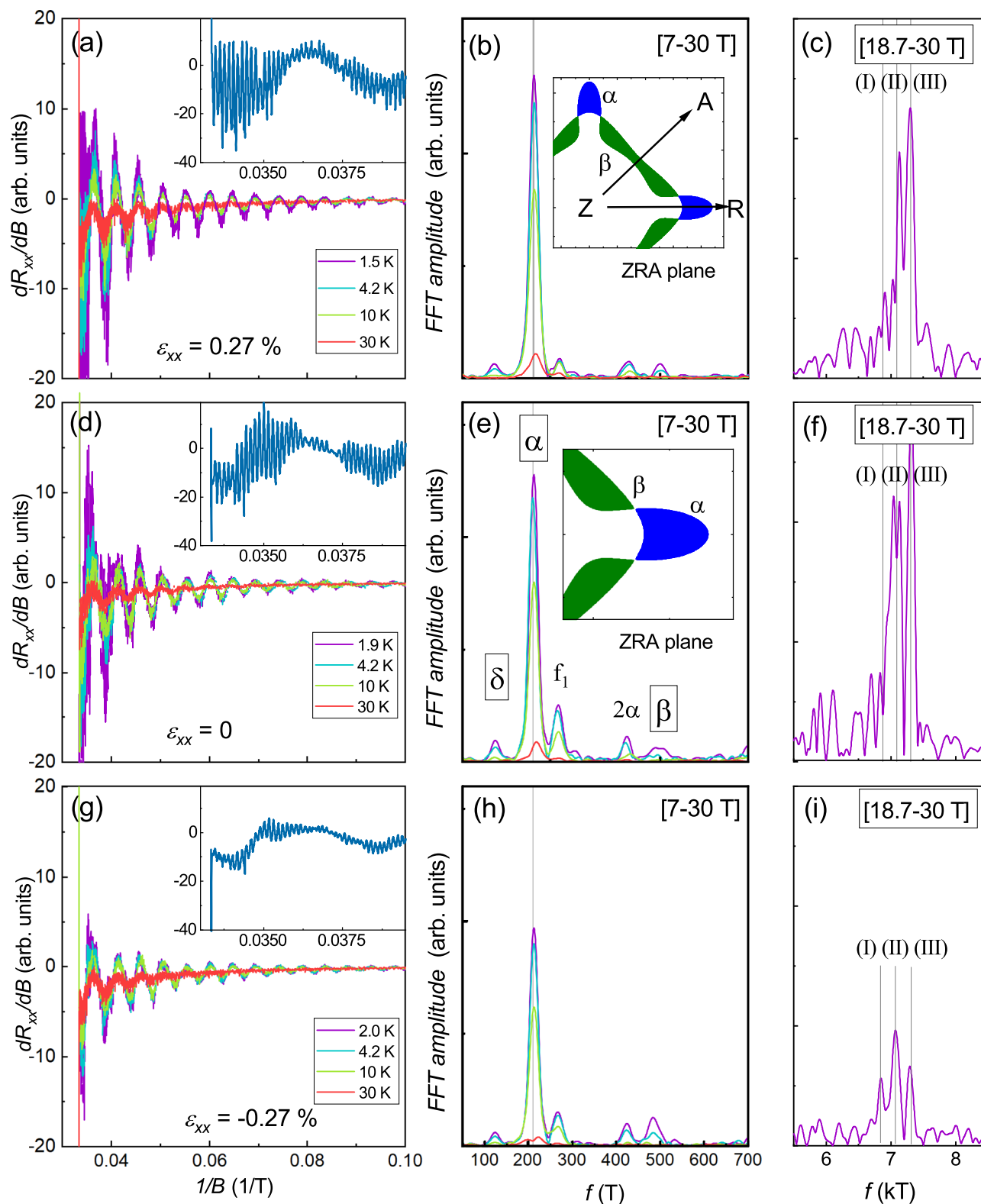


Fig. 3 | QO spectra and fast Fourier transforms for S2[100]. a, d, g dR_{xx}/dB as a function of $1/B$. The insets show a zoom into the high-frequency part for the lowest temperature. The corresponding FFTs for $f < 700$ T (b, e, h) and for the high-frequency MB oscillations (c, f, i) for maximum tensile strain, 0.27% (a–c), zero strain (d–f), and

maximum compressive strain, -0.27% (g–i). The vertical lines in (c, f, i) indicate the α -separation between the high-frequency peaks (I–III) of the spectrum for the lowest temperature. In total ten temperatures are measured, and only four are shown for clarity. The inset of (b) and (e) show a schematic of the ZRA plane of the FS.

420 T, and 475 T. The frequency at 420 T corresponds to 2α and we assign the frequency at 475 T to the β -orbit. Consequently, $f_1 = f_{\beta-\alpha}$ indicating possible MB, i.e., quasi-particle tunneling between the adjacent α and β pockets in momentum space^{41–43}. As can be seen in the derivative of the raw

data, the QO spectrum for zero strain is altered in the presence of tensile or compressive strain, see Fig. 3b, h, respectively. While the amplitude of the α -orbit decreases under compressive strain, the one for the β -orbit becomes more pronounced. The FFT amplitude for the MB orbit f_1 becomes less

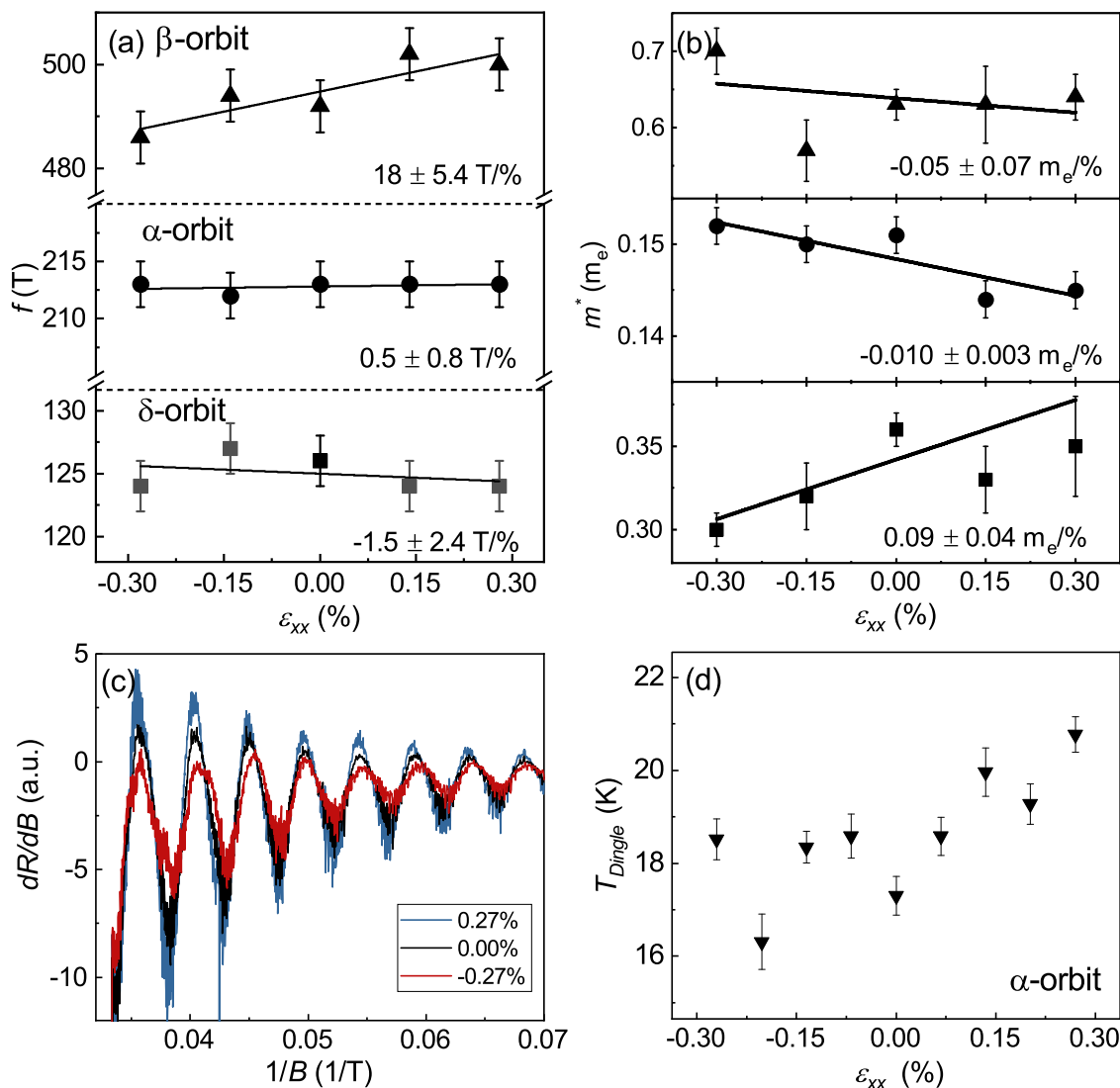


Fig. 4 | QO analysis. **a** Frequencies and **b** extracted quasi-particles cyclotron masses and **c** dR_{xx}/dB for maximum compressive, tensile, and zero strain as a function of $1/B$. **d** Dingle temperature T_D for the α -orbit as a function of uniaxial strain ϵ_{xx} . Note that, the Dingle temperature is extracted from the Dingle field with constant mass.

pronounced for both tensile and compressive strain. A zoom of the FS in the ZRA-plane, with the α (hole) and β (electron) pocket, is shown in the inset of Fig. 3e.

Next, we discuss the high-frequency QOs which display clear changes in their amplitudes. Their FFTs are presented in the range [18.7–30 T] and illustrated in Fig. 3c, f, i for tensile, zero, and compressive strain at 1.4 K. For compressive strain, Fig. 3i, we observe three distinct and closely spaced peaks at 6830 T, 7040 T, and 7290 T, labeled by Roman numbers I, II, and III. These high-frequency QOs originate from MB most likely in the ZRA-plane of the FS. The distance between these orbits is approximately $f_\alpha = 210$ T between peaks I and II, while the distance between II and III is 265 T, i.e., $f_1 = f_{\beta-\alpha}$. This scenario is analogous to high-frequency QOs found in ZrSi₄⁴¹ and HfSi₄⁴³. The observation of both the f_1 frequency and the spacing of the high f MB in the ZRA-plane rule out the possibility of a closed inner and outer pocket in ZrSiSe^{30,32}. While compared to compressive strain, the FFT amplitudes are strongly enhanced at zero and tensile strain, no longer clear separation is found between peaks I and II. Peak III becomes the most pronounced while its frequency (area in k -space) is unaffected.

The QO frequencies and extracted quasi-particle masses for the individual orbits α , β and δ are plotted as a function of uniaxial strain in Fig. 4a, b. The frequency and cyclotron mass m_c of the α -orbit at zero strain are in agreement with literature³⁹. Although f_α remains constant, its mass slightly

decreases (increases) under tensile (compressive) strain. f_β slightly increases (decreases) under tensile (compressive) strain with its mass being rather constant under strain. f_δ remains constant but shows an increase (decrease) in its m_c for tensile (compressive) strain. The lack of evidence for a change in m^* from our QO experiments indicates that the application of strain in ZrSiSe primarily affects the scattering time. The frequency $f_1 = f_{\beta-\alpha}$ seems to be in the order of change of β again indicating this frequency is likely to originate from MB between the α and β frequency.

Lastly, we have a closer look at the QO frequency and amplitude of the α -orbit, the dominant frequency in the entire range of magnetic fields. As discussed already, we observe a negligible change in frequency when comparing tensile and compressive strain, see Fig. 4c. The FFT amplitude, however, decreases (increases) for maximum compressive (tensile) strain compared to $\epsilon_{xx} = 0$. From the envelope function of the QOs associated with the α -orbit, we extract the Dingle temperature T_D which is inversely proportional to the quantum lifetime. We then plot its value as a function of ϵ_{xx} in Fig. 4d, highlighting an increase in T_D for tensile and a decrease in T_D for compressive strain.

The ratio between τ_{tr}/τ_q is different for various classes of quantum materials. With this strain study, we trace strain-induced changes in both transport mobility and quantum mobility. In Fig. 2e a monotonic increase of the mean transport lifetime as a function of strain is observed. The quantum

mobility μ_α of the alpha pocket, which depends on T_D and m^* , shows a positive trend from compressive to tensile strain within our experimental resolution.

The decrease in quantum lifetime for compressive strain coincides with the decrease in amplitude of the high-frequency breakdown. This might be due to the decrease of the area of the β -pocket (f_β), increasing the distance between the apex of the α and β pocket. Another origin might be a change in the curvature of the pockets leading to a change in the local scattering rate.

We finally compare our magneto-transport results under uniaxial strain to high-pressure magneto-transport experiments performed on ZrSiS^{45,46}. Van Gennep, et al. find an increase in the magnitude of the high-field resistivity from zero to 1.7 GPa⁴⁵. They also observe QOs originating from two extremal orbits of the FS of ZrSiS. While the high-frequency QOs, corresponding to the α (hole) pocket in ZrSiS and ZrSiSe only change by 2%, the low-frequency QOs change by 15%. This low-frequency orbit has not been found in ZrSiSe. It has been proposed that the change in phase of the low-frequency QO may originate from a possible pressure-induced topological quantum phase transition⁴⁵. Gu et al. find that applying hydrostatic pressures up to 7.4 GPa does not alter the MR and the amplitude of the QOs in magnetic fields up to 27.5 T⁴⁶. However, larger hydrostatic pressure leads to a strong decrease in both the MR accompanied by an abrupt increase in the zero-field resistivity related to a strong drop in transport mobility. Gu et al. also follow the evolution of quasi-particles residing on the α pocket with increasing pressure. They find a sudden increase of m_α^* accompanied by a drop in the quantum mobility of the carriers above 7.4 GPa. Furthermore, they observe a phase change from a non-trivial to a trivial phase with increasing pressure. They attribute these changes to a pressure-induced phase transition induced by inhomogeneous compression leading to changes in the crystal symmetries and destruction of the nodal-line state⁴⁶. In contrast to high-pressure studies, our magneto-transport experiments under uniaxial strain show a continuous tunability of the transport and quantum mobilities while a strain-induced phase transition has not been found in the range of applied uniaxial strain.

In summary, we have demonstrated that MER in compensated semimetals can be described by using a classical two-carrier Drude model. By plotting the MER as a function of the applied magnetic field, these experiments allow one to directly visually distinguish between changes in the compensation ratio and/or the transport mobility of charge carriers. For ZrSiSe, changes in the transport mobility of the quasi-particles account for the observed changes in the MR under uniaxial strain. Concomitantly, we have shown that uniaxial strain alters the quasi-particle properties and MB in the ZRA-plane of the FS, as revealed in the QO spectra.

Methods

Samples synthesis

Single crystals of ZrSiSe were grown by placing stoichiometric amounts of the individual elements and a small amount of I_2 inside a carbon-coated quartz tube, which was sealed under vacuum and heated to 1100 °C with a 100 °C temperature gradient for one week. Subsequently, the obtained crystals were annealed at 600 °C for a period of four weeks. SEM/EDX experiments were employed to confirm the exact composition.

Transport experiments under uniaxial strain

The ZrSiSe crystals were cut into $1-1.5 \times 0.25 \times 0.1$ mm³ bars using a wire saw and four electrical contacts (titanium: 7 nm, gold: 70 nm) were evaporated prior to the experiments. Each individual sample was clamped onto the Razorbill CS100 strain cell⁴ using blue Araldite glue for maximum strain transfer, see the insets in Fig. 1a. The applied strain ϵ_{xx} is measured via a capacitive measurement of the displacement in the strain cell. In total, five ZrSiSe samples—three cuts along the [100] and two along the [110] direction—with a residual resistance ratio of 30–40 were measured all showing a similar decrease (increase) of 4–8% in MR under maximum compressive (tensile) strain. The longitudinal resistance, R_{xx} , has been measured using a standard lock-in technique (13 Hz).

Data availability

Correspondence and requests for materials should be addressed to Steffen Wiedmann.

Received: 5 January 2024; Accepted: 17 July 2024;

Published online: 20 August 2024

References

1. Worasaran, T. et al. Nematic quantum criticality in an Fe-based superconductor revealed by strain-tuning. *Sci. Adv.* **372**, 973–977 (2021).
2. Mutch, J. et al. Evidence for a strain-tuned topological phase transition in ZrTe₅. *Sci. Adv.* **5**, eaav9771 (2019).
3. Straquadine, J. et al. Evidence for realignment of the charge density wave state in ErTe₃ and TmTe₃ under uniaxial stress via elastocaloric and elastoresistivity measurements. *Phys. Rev. X* **12**, 021046 (2022).
4. Hicks, C. W. et al. Piezoelectric-based apparatus for strain tuning. *Rev. Sci. Instrum.* **85**, 065003 (2014).
5. Ghosh, S. et al. Piezoelectric-driven uniaxial pressure cell for muon spin relaxation and neutron scattering experiments. *Rev. Sci. Instrum.* **91**, 10 (2020).
6. Ikeda, M. S. et al. AC elastocaloric effect as a probe for thermodynamic signatures of continuous phase transitions. *Rev. Sci. Instrum.* **90**, 083902 (2019).
7. Cenker, J. et al. Reversible strain-induced magnetic phase transition in a van der Waals magnet. *Nat. Nanotechnol.* **17**, 256–261 (2022).
8. Singleton, J. Temperature scaling behavior of the linear magnetoresistance observed in high-temperature superconductors. *Phys. Rev. Mater.* **4**, 061801 (2020).
9. Hayes, I. et al. Scaling between magnetic field and temperature in the high-temperature superconductor BaFe₂(As_{1-x}P_x)₂. *Nat. Phys.* **12**, 916–919 (2016).
10. Khouri, T. et al. Linear magnetoresistance in a quasifree two-dimensional electron gas in an ultrahigh mobility GaAs quantum well. *Phys. Rev. Lett.* **117**, 256601 (2016).
11. Ali, M. et al. Large, non-saturating magnetoresistance in WTe₂. *Nature* **514**, 205–208 (2014).
12. Shekhar, C. et al. Extremely large magnetoresistance and ultrahigh mobility in the topological Weyl semimetal candidate NbP. *Nat. Phys.* **11**, 645–649 (2015).
13. Sun, S. et al. Large magnetoresistance in LaBi: origin of field-induced resistivity upturn and plateau in compensated semimetals. *New J. Phys.* **18**, 082002 (2016).
14. Tafti, F. et al. Resistivity plateau and extreme magnetoresistance in LaSb. *Nat. Phys.* **12**, 272–277 (2016).
15. Fauqué, B. et al. Magnetoresistance of semimetals: the case of antimony. *Phys. Rev. Mater.* **2**, 114201 (2018).
16. Kumar, N. et al. Extremely high magnetoresistance and conductivity in the type-II Weyl semimetals WP₂ and MoP₂. *Nat. Commun.* **8**, 1642 (2017).
17. Chiu, Y.-C. et al. Origin of the butterfly magnetoresistance in a Dirac nodal-line system. *Phys. Rev. B* **100**, 125112 (2019).
18. Kaganov, M. & Lifshits, I. M. Electron theory of metals and geometry. *Sov. Phys. Usp.* **22**, 904 (1979).
19. Jo, N. H. et al. Magnetoelastoresistance in WTe₂: exploring electronic structure and extremely large magnetoresistance under strain. *Proc. Natl. Acad. Sci. USA* **116**, 25524–25529 (2019).
20. Yang, J. et al. Elastic and electronic tuning of magnetoresistance in MoTe₂. *Sci. Adv.* **3**, eaao4949 (2017).
21. Neupane, M. et al. Observation of topological nodal fermion semimetal phase in ZrSiS. *Phys. Rev. B* **93**, 201104(R) (2016).
22. Wang, X. et al. Evidence of both surface and bulk Dirac bands and anisotropic non-saturating magnetoresistance in ZrSiS. *Adv. Electron. Mater.* **2**, 1600228 (2016).

23. Ali, M. et al. Butterfly magnetoresistance, quasi-2D Dirac Fermi surface and topological phase transition in ZrSiS. *Sci. Adv.* **2**, e1601742 (2016).
24. Schoop, L. M. et al. Dirac cone protected by non-symmorphic symmetry and three-dimensional Dirac line node in ZrSiS. *Nat. Commun.* **7**, 11696 (2016).
25. Singha, R. et al. Large nonsaturating magnetoresistance and signature of nondegenerate Dirac nodes in ZrSiS. *Proc. Natl. Acad. Sci. USA* **114**, 2468 (2017).
26. Matusiak, M. et al. Thermoelectric quantum oscillations in ZrSiS. *Nat. Commun.* **8**, 15219 (2017).
27. Zhang, L. et al. Comprehensive investigation of quantum oscillations in semimetal using an ac composite magnetoelectric technique with ultrahigh sensitivity. *npj Quant. Mater.* **9**, 11 (2024).
28. Liu, X. et al. Quantum transport of the 2D surface state in a nonsymmorphic semimetal. *Nano Lett.* **21**, 4887–4893 (2021).
29. Fereidouni, A. et al. Enhancement of 2D topological semimetal transport properties by current annealing. *Appl. Phys. Lett.* **121** (2022).
30. Pan, H. et al. Three-dimensional anisotropic magnetoresistance in the Dirac node-line material ZrSiSe. *Sci. Rep.* **8**, 9340 (2018).
31. Shirer, K. R. et al. Out-of-plane transport in ZrSiS and ZrSiSe microstructures. *APL Mater.* **7**, 101116 (2019).
32. Song, J. et al. Kohler's rule and anisotropic Berry-phase effect in nodal-line semimetal ZrSiSe. *J. Appl. Phys.* **131**, 065106 (2022).
33. Scherer, M. et al. Excitonic instability and unconventional pairing in the nodal-line materials ZrSiS and ZrSiSe. *Phys. Rev. B* **98**, 241112 (2018).
34. Shao, Y. et al. Electronic correlations in nodal-line semimetals. *Nat. Phys.* **16**, 636–641 (2020).
35. Rendy, B. & Hasdeo, E. H. Strain effects on band structure and Dirac nodal-line morphology of ZrSiSe. *J. Appl. Phys.* **129**, 014306 (2021).
36. Chen, F. et al. Temperature-induced Lifshitz transition and possible excitonic instability in ZrSiSe. *Phys. Rev. Lett.* **124**, 236601 (2020).
37. Dong, E. et al. Pressure-induced electronic and structural transition in nodal-line semimetal ZrSiSe. *Inorg. Chem.* **60**, 11140–11146 (2021).
38. Gatti, G. et al. Light-induced renormalization of the Dirac quasiparticles in the nodal-line semimetal ZrSiSe. *Phys. Rev. Lett.* **125**, 076401 (2020).
39. Hu, J. et al. Evidence of topological nodal-line fermions in ZrSiSe and ZrSiTe. *Phys. Rev. Lett.* **117**, 016602 (2016).
40. Pezzini, S. et al. Unconventional mass enhancement around the Dirac nodal loop in ZrSiS. *Nat. Phys.* **14**, 178–183 (2018).
41. Müller, C. S. A. et al. Determination of the Fermi surface and field-induced quasiparticle tunneling around the Dirac nodal loop in ZrSiS. *Phys. Rev. Res.* **2**, 023217 (2020).
42. Van Delft, M. et al. Electron-hole tunneling revealed by quantum oscillations in the nodal-line semimetal HfSiS. *Phys. Rev. Lett.* **121**, 256602 (2018).
43. Müller, C. S. A. et al. Field-induced quasi-particle tunneling in the nodal-line semimetal HfSiS revealed by de Haas-van Alphen quantum oscillations. *Phys. Rev. Res.* **4**, 043008 (2022).
44. Shoenberg, D. (ed) *Magnetic Oscillations in Metals* (Cambridge Univ. Press, 1984).
45. Van Gennep, D. et al. Possible pressure-induced topological quantum phase transition in the nodal line semimetal ZrSiS. *Phys. Rev. B* **99**, 085204 (2019).
46. Gu, C. C. et al. Experimental evidence of crystal symmetry protection for the topological nodal line semimetal state in ZrSiS. *Phys. Rev. B* **100**, 205124 (2019).

Acknowledgements

This work was supported by HFML-RU/NWO-I, a member of the European Magnetic Field Laboratory (EMFL), and by the UK Engineering and Physical Sciences Research Council (grant no. EP/N01085X/1). It is part of the project TOPCORE (OCENW.GROOT.2019.048) of the research program NWO-GROOT which is financed by the Dutch Research Council (NWO). L.M.S. was supported by the Princeton Center for Complex Materials, a National Science Foundation (NSF)-MRSEC program (DMR-2011750), and the Gordon and Betty Moore Foundation's EPIQS initiative (grant no. GBMF9064).

Author contributions

J.F.L., A.K., and J.P.L. conducted the high-field magneto-transport experiments under uniaxial strain supported by A.V. and S.W. Samples have been grown by R.S. and L.M.S. J.F.L. analyzed the data with input from A.K., C.S.A.M., and M.R.D. A.V., N.E.H., and S.W. conceived the project. All authors were involved in the discussion and interpretation of the results. J.F.L. and S.W. wrote the manuscript with input from all co-authors.

Competing interests

The authors declare no competing interests.

Additional information

Supplementary information The online version contains supplementary material available at <https://doi.org/10.1038/s41535-024-00670-2>.

Correspondence and requests for materials should be addressed to J. F. Linnartz or S. Wiedmann.

Reprints and permissions information is available at <http://www.nature.com/reprints>

Publisher's note Springer Nature remains neutral with regard to jurisdictional claims in published maps and institutional affiliations.

Open Access This article is licensed under a Creative Commons Attribution 4.0 International License, which permits use, sharing, adaptation, distribution and reproduction in any medium or format, as long as you give appropriate credit to the original author(s) and the source, provide a link to the Creative Commons licence, and indicate if changes were made. The images or other third party material in this article are included in the article's Creative Commons licence, unless indicated otherwise in a credit line to the material. If material is not included in the article's Creative Commons licence and your intended use is not permitted by statutory regulation or exceeds the permitted use, you will need to obtain permission directly from the copyright holder. To view a copy of this licence, visit <http://creativecommons.org/licenses/by/4.0/>.

© The Author(s) 2024, corrected publication 2024